Dalton Transactions

Accepted Manuscript

ROYAL SOCIETY OF CHEMISTRY

www.rsc.org/dalton

Journal Name

ARTICLE

Fluoride solid electrolytes: investigation of the tysonite-type solid solutions $La_{1-x}Ba_xF_{3-x}$ ($x < 0.15$)

Received 00th January 20xx,
Accepted 00th January 20xx

DOI: 10.1039/x0xx00000x

www.rsc.org/

Johann Chable,[a,b] Belto Dieudonné,[a] Monique Body,[b] Christophe Legein,[b] Marie-Pierre Crosnier-Lopez,[b] Cyrille Galven,[b] Fabrice Mauvy,[a] Etienne Durand,[a] Sébastien Fourcade,[a] Denis Sheptyakov,[c] Marc Leblanc,[b] Vincent Maisonneuve,[b] and Alain Demourgues*[,a]

Pure tysonite $La_{1-x}Ba_xF_{3-x}$ solid solutions for $x < 0.15$ were prepared by solid state synthesis in a platinum tube under azote atmosphere with subsequent quenching for $0.07 \le x < 0.15$. The solid solutions were studied by X-ray, electron and neutron diffractions and by ^{19}F NMR and impedance spectroscopies. The evolutions of the cell parameters obeying Vegard's rule were determined for $0 < x \le 0.15$ and atomic position parameters were accurately refined for x = 0.03, 0.07 and 0.10. The chemical pressure induced by large Ba^{2+} cations leads to an increase of the unit cell parameters. Fluorine environments and mobilities are discussed on the basis of results of neutron diffraction and ^{19}F solid state NMR. The F1 subnetwork is lacunar; fluorine exchange occurs according to the order: F1-F1 and F1-F2,3. 2D EXSY NMR spectra of $La_{0.97}Ba_{0.03}F_{2.97}$ reveal, for the first time, chemical exchange between F2 and F3 sites that requires two successive jumps. The ionic conductivity was evaluated from sintered pellets and different shaping methods were compared. The only structural features which could explain the conductivity maximum are a crossover together with a smaller dispersion of F1-F1,2,3 distances at x = 0.05-0.07.

Introduction

The need for energy storage, both efficient and sustainable, keeps increasing along with the surge of the number of electric and electronic devices. Different ways have been explored to fulfil this need: either improvement of the current reliable technologies (e.g. Li-ion[1,2] and Ni-MH1) or development of new concepts such as Li-S,[3] Mg-ion,3 Li-air,[4] Na-ion[5] or Fluoride Ion Battery (FIB).[6] The later refers to a solid stack composed of solid fluoride materials as electrodes and electrolyte.[7-9] As a reason of high ionic conductivities of fluoride electrolytes[10,11] at low temperature (i.e. close to room temperature), this all solid concept appeared 40 years ago.7

The CaF_2-fluorite type (*Fm*-3*m*) and the LaF_3-tysonite type (*P*-3*c*1) structures are among the best fluoride electrolytes.[12,13] Their crystallographic networks allow high fluorine ion mobility which can be improved by aliovalent doping. The fluorite-type exhibits numerous interstitial sites which can accept mobile fluorine atoms. As a consequence, a large range of solubility, up to ≈ 50%, occurs in the MF_2-REF_3 chemical systems (M = alkaline-earth and RE = rare earth). At the opposite, the presence of anionic vacancies in the doped tysonite-type structure is responsible of the high conductivity values in these fluorides. LaF_3 (potentially doped by Eu^{2+}) is applied as a fluoride selective electrode (FSE[14]) and as a gas sensor.[15]

For FIB, the electrolyte with the best compromise between high conductivity and electrochemical stability seems to be $La_{1-x}Ba_xF_{3-x}$ ($x \le 0.15$).6 While single crystal studies on LaF_3 by neutron[16] or X-ray diffraction are in good agreement, the crystallographic data on the solid solutions are rather erratic.[17,18] Moreover, the solubility limit of BaF_2 in LaF_3 needs to be ascertained.[19,20] Roos *et al.* have largely investigated the fluorine mobility on $La_{1-x}Ba_xF_{3-x}$ single-crystals: electrical,[21] electronic[22] and ionic[23] conductivities, bulk and interfacial polarization,[24] dielectric relaxation[25] and small-signal ac response.[26] They proposed the first equivalent circuits to model the impedance spectra[24] and they demonstrated that the electronic conductivity can be neglected.[22] The ionic conductivity was found to be anisotropic for LaF_3 below 420 K; its evolution with Ba rate exhibits an optimum around x = 0.07 (3.10^{-4} S.cm^{-1} at 330 K) which has been explained by a percolation threshold for one type of conduction path.[21-25] These conclusions well matched also with those of Sorokin *et al.* extended to numerous other $RE_{1-x}M_xF_{3-x}$ tysonite fluorides.[10,27-33] They found a maxima of conductivity close to x = 0.05 (8.10^{-5} S.cm^{-1} at 293 K) and they also observed that a strontium doping leads to the highest conductivity (3.10^{-4} S.cm^{-1} at 293 K

[a] *ICMCB* UPR *CNRS 9048, 87 avenue du Docteur Schweitzer 33608 PESSAC, France*
[b] *Université du Maine, Institut des Matériaux et des Molécules du Mans (IMMM), UMR CNRS 6283, avenue O. Messiaen 72085 Le Mans, France*
[c] *Laboratory for Neutron Scattering and Imaging, Paul Scherrer Institut, 5232 Villigen PSI, Switzerland*
[d] **Corresponding author: alain.demourgues@icmcb.cnrs.fr*

Electronic Supplementary Information (ESI) available: XRD patterns of $La_{1-x}Ba_xF_{3-x}$, Synthesis conditions, XRD Rietveld refinement of $La_{0.95}Ba_{0.05}F_{2.95}$, Neutron diffraction refinements models, Neutron diffraction patterns, Interatomic distances, Cell parameters evolution, ^{19}F MAS NMR spectra of $La_{1-x}Ba_xF_{3-x}$, RT-conductivity vs x, Nyquist diagram (non-sintered pellet), Equivalent capacity and frequency diagrams (sintered pellet), Cif files. See DOI: 10.1039/x0xx00000x

for $La_{0.95}Sr_{0.05}F_{2.95}$). Additionally, they pointed out that sintered pellets allow to reach conductivity values close to those of single crystals. For x > 0.05, the decrease of ionic conductivity is probably related to the creation of defects clusters.[28,29] Recently, Fichtner *et al.* observed a conduction maximum at x = 0.1 for mechanosynthesized powders6 and thin films[34] and that the absence of sintering is detrimental to the conductivity.[35]

The last aspect of $La_{1-x}Ba_xF_{3-x}$ characterization concerns ^{19}F NMR experiments, particularly useful to probe accurately the environments and mobilities of fluoride ions. In the tysonite structure (*P*-3*c*1), three crystallographic fluorine sites with different occupancies are occupied (F1 (12g), F2 (4d) and F3 (2a)). Interpretation of fluorine conductivity has greatly evolved since the early results of Aalders *et al.* on LaF_3 or $La_{1-x}Ba_xF_{3-x}$.[36,37] From relaxation time measurements, they concluded that F2-F3 sublattices govern the low temperature ionic conductivity. Calculations of probability density functions (PDFs) led Brach and Schulz to identify three different probability jumps for LaF_3: F1-F1 and F3-F3 > F1-F3-F1.[38] The study of Privalov *et al.* on $La_{1-x}Sr_xF_{3-x}$[39-42] (0 < x < 0.16 and 130 K < T < 520 K) demonstrated that fluorine diffusion starts on the F1 sublattice and that the increase of the F1/F2,3 peak intensity ratio along with the shift of the F1 peak position imply the probability jump order: F1-F1 > F1-F2,3 > F2,3-F2,3. The activation temperature of the jumps decreases to a minimum with the doping rate (x ≈ 0.05) which corresponds to the maximum of ionic conductivity. From high-resolution ^{19}F MAS NMR study at variable temperature (300 K < T < 540 K) on LaF_3 and $La_{0.99}Sr_{0.01}F_{2.99}$, Wang and Grey showed that the three crystallographic sites have very different mobilities and that the different fluoride-ion jump pathways are thermally activated in the order: F1-F1 < F1-F3 < F1-F2.[43] In the light of previous studies mainly obtained from LaF_3, SrF_2-doped LaF_3 or very slightly BaF_2-doped LaF_3, it appears that anionic vacancies seem to be preferentially located on the F1 sublattice.[40,41,44]

It must be noted that most of previous works have been performed on single-crystals whereas the shaping effects of polycrystalline powders, better suited as battery components, have not drawn a lot of attention. Moreover, accurate structural data on $La_{1-x}Ba_xF_{3-x}$ are still missing and solubility limits are not well defined at low temperatures. A comprehensive study of $La_{1-x}Ba_xF_{3-x}$ with 0 < x ≤ 0.15, prepared by conventional solid state synthesis, is reported here. The ionic conductivity is compared for various pellet shaping methods. Fluorine environments and mobilities are discussed from neutron diffraction and ^{19}F solid state NMR data.

Experimental

2.1 Powder synthesis

Microcrystalline $La_{1-x}Ba_xF_{3-x}$ powders were prepared by solid state synthesis, starting from stoichiometric mixtures of LaF_3 (Alfa Aesar 99.99% anhydrous REO) and BaF_2 (Stem 99.99% Puratrem). Precursors were grinded in an agate mortar during 30 minutes in a glovebox under purified N_2 atmosphere. They were then inserted in platinum tubes and dried under secondary vacuum at 150°C. Tubes were sealed by arc melting and heated in a Nabertherm muffle furnace. Details of synthesis are given as ESI. The resulting products, lightly sintered, were milled again during 30 minutes.

2.2 X-ray and neutron diffraction

XRD analyses were performed with a PANalytical (X'Pert Pro) diffractometer (Cu Kα radiation). The EVA software was used for phase identification. Cell parameters were determined from Rietveld refinements using Highscore (X'Pert Pro).

$La_{0.97}Ba_{0.03}F_{2.97}$, $La_{0.93}Ba_{0.07}F_{2.93}$ and $La_{0.90}Ba_{0.10}F_{2.90}$ neutron diffraction patterns were collected from ~4 g samples at 300 K with the HRPT diffractometer at SINQ at Paul-Scherrer Institute, Switzerland under the following conditions: λ = 1.494 Å, 2θ range 3.5°–164.70°, step size 0.05°. Rietveld refinements were performed with the Fullprof Suite programs and the Thompson-Cox-Hastings profile function was applied.

Further details on the experimental crystal structures may be obtained as **ESI** and from the Fachinformationszentrum Karlsruhe, 76344 Eggenstein-Leopoldshafen, Germany (Fax: +49 7247808666; email: crysdata@fiz-karlsruhe.de), on quoting the depositories no. CSD-429735, CSD-429736 and CSD-429737, respectively.

2.3 Transmission Electron Microscopy (TEM)

Selected Area Electron Diffraction (SAED) were carried out on a JEOL 2100 electron microscope operating at 200 kV and equipped with a side entry ± 35° double tilt specimen holder. Chemical analysis is done on a large number of crystallites with an Energy Dispersive X-ray (EDX) spectrometer JEOL JED-2300T coupled with the TEM. Samples were prepared by dispersing about 10 mg of powder in ethanol and placing one drop of this suspension on a carbon-coated copper grid to promote random orientation of crystallites.

2.4 ^{19}F Nuclear Magnetic Resonance (NMR)

^{19}F solid state Magic Angle Spinning (MAS) NMR spectra were recorded on an Avance 300 Bruker spectrometer operating at 7 T (^{19}F Larmor frequency of 282.2 MHz), using a 1.3 mm diameter probe head allowing spinning frequencies up to 70 kHz. 1D NMR spectra were acquired using a Hahn echo sequence for which interpulse delay was synchronized with the rotor spinning frequency. A 90° pulse length of 1.55 µs was used, recycle delays of 30 s were applied and 128 transients were accumulated. Due to air frictional heating, the sample temperature varies by up to 32°C from 34 to 64 kHz (^{207}Pb isotropic chemical shift of $Pb(NO_3)_2$ was used as NMR thermometer[45,46]). The maximum temperature gradient over the dimension of the 1.3 mm rotor was estimated around 8°C. Two-dimensional (2D) exchange spectroscopy (EXSY)[47] MAS ^{19}F NMR spectra were acquired at 44 kHz (40°C), allowing rotor synchronisations in both the F1 and F2 directions, and thus avoiding the presence of spinning sidebands in the spectra. A saturation sequence of 3 ms duration was used to ensure repeatability, and the recycle delay value was set to 5 s. Mixing times ranging from 100 µs to 5 ms were used. A total of 100

rotor-synchronized t1 increments with 48 transients each were accumulated and phase sensitive detection in the indirect dimension was achieved using the States method.[48] The ^{19}F chemical shifts are referenced to $CFCl_3$ at 0 ppm. Spectra reconstructions were achieved using the DMFIT software.[49]

2.5 Pellet-shaping process

Three shaping techniques were applied: uniaxial-pressing (UP–1 ton, 1 min, Specac handpress), isostatic-pressing (IP–5 kbar, 5 min, TopIndustrie Press) and sintering in sealed Pt tubes (S–N_2, 900°C, 24 h). Pellets of 5 mm diameter and ca. 2.5 mm thickness were prepared for the Electrochemical Impedance Spectroscopy (EIS) measurements using separately or successively these three techniques (UP, IP and S) on the same batch. For $x > 0.05$, pellet composition was checked by XRD and EDX analyses after sintering.

2.6 Electrochemical Impedance Spectroscopy (EIS)

Ionic conductivity was measured by Electrochemical Impedance Spectroscopy (EIS) on the shaped pellets coated on both sides with Pt as ion-blocking electrodes. The dimensions and mass of pellets were determined geometrically before each EIS measurement to evaluate compactness. The conductivity measurements for sintered pellets were performed when the relative density was at least equal to 90%. All measurements were performed from 25°C to 250°C under nitrogen. Impedance data were collected under steady state conditions within the frequency range of 1 MHz-1Hz (50-100 mV amplitude) using a Solartron 1260 device. The linear response domain of the samples was systematically checked by excitation at different amplitudes (50, 70 and 100 mV) and the stationary state before and after at least 1 h at 50°C. The impedance data reported in a Nyquist diagrams were fitted with the Zview software (Scribner Associates).

Results and Discussion

3.1 X-ray and electron diffractions

Pure $La_{1-x}Ba_xF_{3-x}$ tysonite phases were obtained for $x \leq 0.05$ with the classical solid state route at 900°C during 24 h **(see ESI)**.

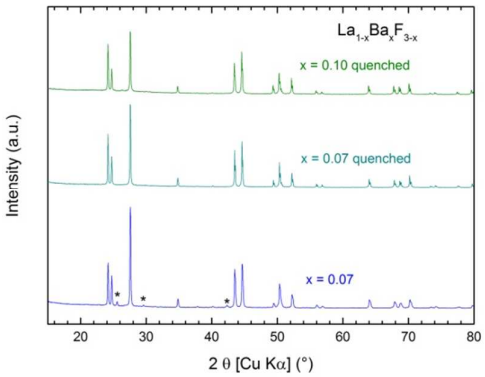

Fig. 1 XRD patterns of $La_{0.93}Ba_{0.07}F_{2.93}$ and $La_{0.90}Ba_{0.10}F_{2.90}$. Stars indicate the peaks of the $Ba_{1-y}La_yF_{2+y}$ fluorite impurity.

Table 1 Cell parameters of $La_{1-x}Ba_xF_{3-x}$ tysonite phases obtained from XRD patterns by Rietveld refinements.

x	a (Å)	c (Å)
0	7.1881(1)	7.3522(2)
0.03	7.1976(2)	7.3639(3)
0.05	7.2090(3)	7.3745(3)
0.07	7.2150(2)	7.3822(3)
0.10	7.2281(3)	7.3966(4)
0.117	7.2342(2)	7.4040(3)
0.142	7.2409(2)	7.4147(3)

For $x \geq 0.07$, a systematic contamination with the $Ba_{1-y}La_yF_{2+y}$ fluorite type phase was observed (**Fig. 1**). Then, the solubility limit is probably reached for $0.05 < x < 0.07$ at T = 900°C. For $La_{0.90}Ba_{0.10}F_{2.90}$, longer durations of grinding and/or annealing (up to 168 h) only reduced the amount of fluorite impurity to 4 wt%. Thereby, higher temperatures and longer times of synthesis completed by a quenching step in water were applied for $x > 0.05$ in order to overpass the previous solubility limit (see **ESI**). Then, pure tysonite phases were obtained for $x = 0.07$ and $x = 0.10$ (**Fig. 1**). Above $x = 0.10$ and even at T = 1350°C, all samples were contaminated by a fluorite impurity: 0.5 and 1.5 wt% for $x = 0.12$ and $x = 0.15$ respectively; the corrected compositions of the tysonite phases are given in **Table 1**. The calculations were performed with the estimated composition of fluorite $Ba_{0.55}La_{0.45}F_{2.45}$ deduced from the cell parameters.[50] It must be noted that the last composition is close to the solubility limit at the eutectic temperature ($x = 0.15$ at 1365°C[19]). Refinements of the XRD patterns by the Rietveld method using Highscore software[51] led to satisfactory fits and the cell parameters were accurately determined (**Table 1**). The values for $x = 0.05$ were confirmed by Rietveld refinement using Fullprof program (**ESI**).[52] According to the so-called Vegard's law, the a and c parameters increase linearly with x **(Fig. 2)**. This evolution is consistent with the values of cation radii in nine-fold coordination (La^{3+} r = 1.356 Å; Ba^{2+} = 1.61 Å).[53] In the tysonite-type network, F2,3 form $_\infty[La_{1-x}Ba_xF]^{2-x}$ layers at z = ¼ (**Fig. 3**); F3 atoms occupy the centers of cationic triangles with D_{3h} point symmetry and F2 atoms are above or below cationic triangles with C_{3v} point symmetry. F1 atoms in $_\infty[F_{2-x}]^{-2+x}$ slabs appear between the F2,3 layers and occupy off-centered positions in cationic distorted tetrahedral sites.

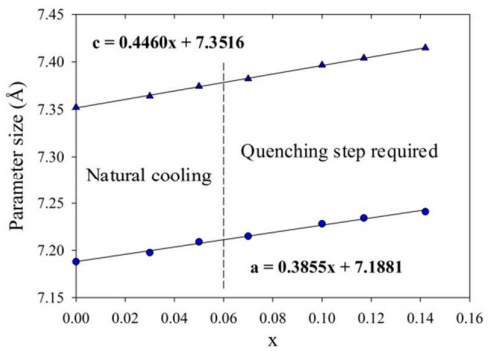

Fig. 2 Evolution with x of the cell parameters of $La_{1-x}Ba_xF_{3-x}$. The straight lines show the linear regressions (equations are given).

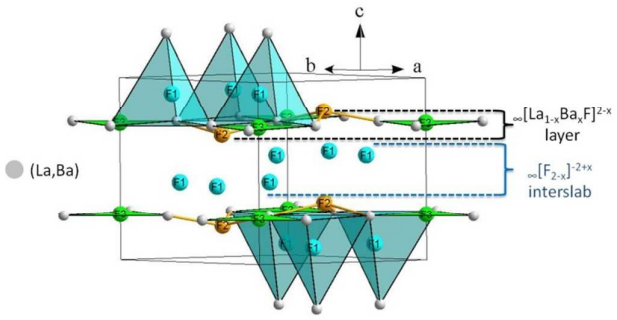

Fig. 3 Representation of the tysonite-type structure with the local environment of F1 (distorted tetrahedral symmetry), F2 (C_{3v} point group) and F3 (D_{3h} point group) atoms, the $_\infty[La_{1-x}Ba_xF]^{2-x}$ layers at z = ¼-¾ and the $_\infty[F_{2-x}]^{-2+x}$ interslab.

The large Ba^{2+} cations exert a chemical pressure which contributes to enlarge the cell parameters. This effect is different for smaller alkaline earth cations such as Ca^{2+} and Sr^{2+} for which the cell volume decreases and remains constant, respectively.[54,55] Then, the consequence on the F local environments and their influence on the F ionic conductivity are different.

TEM experiments were performed on $La_{0.97}Ba_{0.03}F_{2.97}$ and $La_{0.95}Ba_{0.05}F_{2.95}$ to check the homogeneity of samples and the presence or absence of any amorphous impurity and/or crystallographic superstructure. EDX analyses carried out on numerous crystallites revealed systematically the simultaneous presence of lanthanum and barium and provided consistent Ba/La molar ratios (3/97 and 5/95, respectively). No trace of oxygen was detected. The reconstitutions of reciprocal space on $La_{0.95}Ba_{0.05}F_{2.95}$ are in good agreement with the characteristic hexagonal cell without highlighting a superstructure.

Moreover, all the observed reflections can be indexed according to the existence conditions of the *P*-3*c*1 tysonite space group (**Fig. 4**).

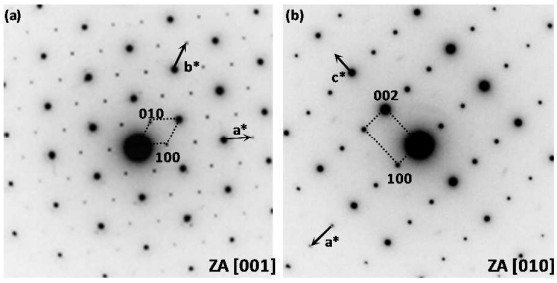

Fig. 4 Typical SAED patterns of $La_{0.95}Ba_{0.05}F_{2.95}$ with two different zone axis.

3.2 Neutron diffraction

Refinements of neutron diffraction patterns were performed by Rietveld method on three samples with x = 0.03, 0.07 and 0.10. Several models of refinements were first tested on $La_{0.90}Ba_{0.10}F_{2.90}$ diagram for fluorine atoms in 12g, 4d and 2a crystallographic sites: isotropic or anisotropic displacement parameters, homogenous or inhomogenous repartition of fluorine vacancies (occupancy rates) (see **ESI**).

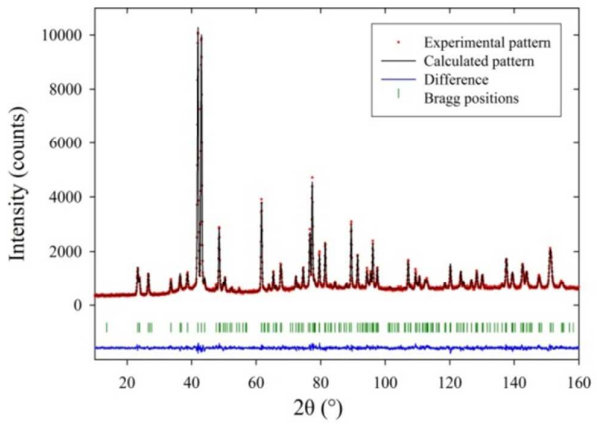

Fig. 5 Experimental and calculated neutron patterns of $La_{0.90}Ba_{0.10}F_{2.90}$ powder.

According to the Hamilton test, the best refinement was obtained with vacancies located on F1 site (12g) only (**Table 2**). A very good match between the experimental and calculated diagrams was observed with low reliability factors: R_p = 12.4, R_{wp} = 10.9 and R_{Bragg} = 3.2 (**Fig. 5**). This resulting model was applied for x = 0.03 and x = 0.07 (see **ESI**). It must be noted that the neutron and X-ray cell parameters line up very well (see **ESI**). The atomic positions together with equivalent displacement parameters are gathered in **Table 2** and interatomic distances are given as **ESI**. Cif files are available from Inorganic Crystal Structure Database (#CSD-429735, CSD-429736 and CSD-429737) and as ESI. All fluorine displacement parameters increase in relation with growing fluorine disorder. It is noteworthy that the largest $B_{eq.}$ values are associated to F1 and F3 atoms which could be related with their mobility (F1-F3 > F1-F2 jump probability).[43]

Table 2 Reliability factors and atomic positions from neutron powder diffraction of the $La_{1-x}Ba_xF_{3-x}$ ($0 \le x \le 0.1$) solid solutions.

La/Ba atom

x_{Ba}	Site	x	y	z	Occ.	$B_{eq.}$ (Å²)
0.03		0.6615 (9)			0.97/0.03	0.72
0.07	6f	0.663 (1)	0	¼	0.93/0.07	0.93
0.10		0.664 (3)			0.90/0.10	0.99

F1 atom

x_{Ba}	Site	x	y	z	Occ.	$B_{eq.}$ (Å²)
0.03		0.363 (1)	0.0502 (6)	0.0811 (6)	0.985	1.82
0.07	12g	0.355 (2)	0.0422 (9)	0.0812 (6)	0.965	3.14
0.10		0.344 (1)	0.034 (1)	0.0815 (2)	0.95	4.06

F2 atom

x_{Ba}	Site	x	y	z	Occ.	$B_{eq.}$ (Å²)
0.03				0.192 (1)	1	1.60
0.07	4d	⅓	⅔	0.198 (2)	1	2.41
0.10				0.2015 (8)	1	2.92

F3 atom

x_{Ba}	Site	x	y	z	Occ.	$B_{eq.}$ (Å²)
0.03					1	3.32
0.07	2a	0	0	¼	1	5.72
0.10					1	6.79

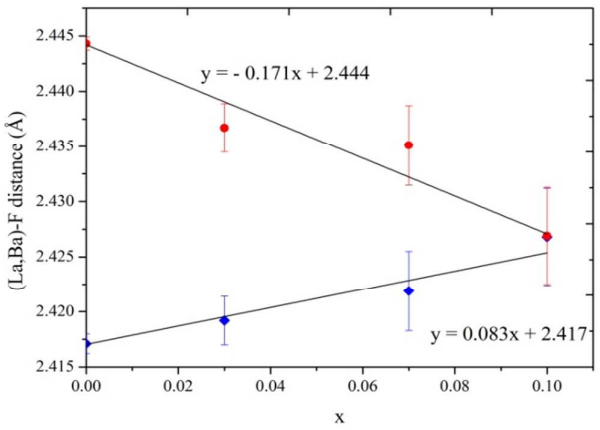

Fig. 6 Evolution of the (La,Ba)-F2 (blue diamonds) and (La,Ba)-F3 (red circles) distances in the $La_{1-x}Ba_xF_{3-x}$ ($0 \le x \le 0.10$) solid solution. Data for LaF_3 are taken from previous work.[16] The straight lines show the linear regressions (equations are given).

Neutron refinements show that vacancies are preferentially located on F1 site, in agreement with early NMR studies.[40,41,44] Moreover, it must be noted that no anomaly affects the evolution of distances and angles. The coordination polyhedron of (La,Ba) atoms is strongly distorted with 7 short (La,Ba)-F distances (2.42-2.54 Å), 2 intermediate distances (2.64-2.75 Å) and 2 long distances (3.00-2.87 Å). Correlatively, the tetrahedral F1 environment is also strongly distorted with 2 short F1-(La,Ba) distances (2.46-2.54 Å), one intermediate distance (2.64-2.74 Å) and one long distance (3.00-2.87 Å). The (La,Ba)-F1-(La,Ba) angle dispersion is quite large and decreases slightly with x from 33.1° to 29.1°.

Compared to the $Sm_{1-x}Ca_xF_{3-x}$ solid solution,[55] the z(F2) coordinate shifts very slightly towards z = ¼ as the substitution rate increases. Thus, the buckling of $_\infty[La_{1-x}Ba_xF]^{2-x}$ layers for Ba-doped compounds is minimum for x = 0.10. (La,Ba)-F2 and (La,Ba)-F3 distances exhibit a slight opposite evolution with x (**Fig. 6**) from 2.417 and 2.443 Å to a similar value (2.427 Å). The longest F-(La,Ba) distances are associated to F1 atoms while the shortest distances are related to F2 and F3 atoms.

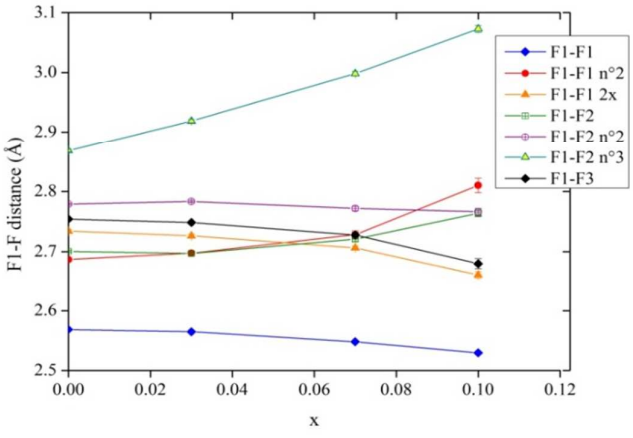

Fig. 7 Evolution of F1-F distances in the $La_{1-x}Ba_xF_{3-x}$ ($0 \le x \le 0.1$) solid solution. Data for LaF_3 are taken from reference.[16]

These distances and the location of vacancies on F1 sites explain that the F1 subnetwork is the main contributor to fluorine mobility. According to the evolution of F2,3-(La,Ba) distances, it can be assumed that the F3 subnetwork contribution to the fluorine mobility is probably higher than that of F2 subnetwork and that both contributions converge for $x \approx 0.10$. The only structural hints to explain the conductivity maximum at $x \approx 0.05$-0.07 is found on the evolution of F1-F distances with a crossover of F1-F1,2,3 distances close to 2.7 Å (**Fig. 7**) together with a smaller dispersion of F1-F1,2,3 distances which could be favourable to F-F jumps.

3.3 ^{19}F Solid State NMR analysis

The $La_{1-x}Ba_xF_{3-x}$ solid solution is also characterized by ^{19}F solid state NMR in order to study the impact of the heterovalent substitution of La^{3+} cations by Ba^{2+} cations on the F^- anions environments and on F^- anion mobilities. The ^{19}F MAS NMR spectra of LaF_3, $La_{0.97}Ba_{0.03}F_{2.97}$, $La_{0.95}Ba_{0.05}F_{2.95}$, $La_{0.93}Ba_{0.07}F_{2.93}$ and $La_{0.90}Ba_{0.10}F_{2.90}$ are reported on **Fig. 8**. The fits of these spectra are reported as **ESI**. As previously reported, the spectrum of LaF_3 can be fitted with three resonances assigned, on the basis of their relative intensities, to the three fluorine crystallographic sites.[43,56] The ^{19}F isotropic chemical shift (δ_{iso}) value decreases when the coordination number (CN) of the fluorine atom increases (δ_{iso}(F2,3) (CN = 3) > δ_{iso}(F1) (CN = 4)) and when the F-La bond lengths increase (δ_{iso}(F2) (2.417 Å)[16] > δ_{iso}(F3) (2.444 Å)[16]). ^{19}F MAS NMR provides an ideal method to probe the local order in fluoride solid solutions.[50,57-64] Nevertheless, the case of the $La_{1-x}Ba_xF_{3-x}$ solid solution seems to be, at first sight, unfavorable since there are three fluorine sites in LaF_3 and since the δ_{iso} value of BaF_2 (-14.3 ppm,[56] CN = 4, 2.683 Å[65]) is in the range of the δ_{iso} values of LaF_3.

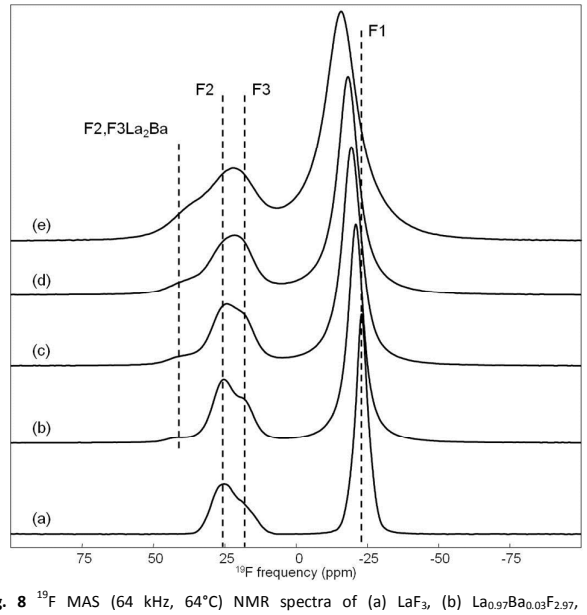

Fig. 8 ^{19}F MAS (64 kHz, 64°C) NMR spectra of (a) LaF_3, (b) $La_{0.97}Ba_{0.03}F_{2.97}$, (c) $La_{0.95}Ba_{0.05}F_{2.95}$, (d) $La_{0.93}Ba_{0.07}F_{2.93}$ and (e) $La_{0.90}Ba_{0.10}F_{2.90}$. The dashed lines indicate the ^{19}F δ_{iso} values of the resonances of F1, F2 and F3 in LaF_3 and of F2 and F3 atoms surrounded by 2 La and 1 Ba atoms in $La_{0.97}Ba_{0.03}F_{2.97}$.

Moreover, local disorder, leading to a broadening of the NMR lines, is expected since the heterovalent substitution generates fluorine vacancies and that both cations have different ionic radii. For x = 0.03 and x = 0.05, the NMR resonances of F2 and F3 remain resolved and a shoulder around 40 ppm is clearly evidenced; its relative intensity increases with x. As expected, the NMR resonance assigned to F1 broadens when x increases and, as recently observed on mecanosynthesized samples,[50,35] moves toward larger chemical shifts (**Fig. 9**).

Such an increase of the chemical shift of the NMR resonance assigned to F1 has been explained either by the substitution of the La atoms coordinating F1 by Ba atoms[50] or by exchange between F1 and F2,3 sublattices.[35] Nevertheless, in these recent studies, the NMR spectra are not fitted and the relative intensities of the NMR resonances are not discussed. Moreover, in ref. [35], these relative intensities are altered from expected populations. The exchange between F1 and F2,3 sublattices is supported by a variable temperature ^{19}F MAS NMR study on LaF_3 and $La_{0.99}Sr_{0.01}F_{2.99}$.[43] Exchange between two sites at a frequency greater than the separation of the two resonances (12.5 kHz between F1 and F2,3 for $La_{0.97}Ba_{0.03}F_{2.97}$) should result in a single resonance whose chemical shift is intermediate between the two resonances.[66] Nevertheless, F1-F1 exchanges being considerably faster (about two order of magnitude in $La_{1-x}Sr_xF_{3-x}$[42]) than F1-F2,3 exchanges, exchange between F1 and F2,3 results in a shift toward larger frequency of the NMR resonance assigned to F1 and in a decrease of the relative intensity of the F2,3 resonances (not resolved on mecanosynthesized samples[50,35]). For x > 0.03, the deviations between expected (from formulation considering fluorine vacancies on F1 site) and estimated (from the fits of the NMR spectra recorded at 64°C) relative intensities of the ^{19}F NMR resonances assigned to F1 and F2,3 (see **Table 3** and **ESI**) demonstrate the occurrence of F1-F2,3 exchanges.

The fraction $((I_{expected} - I_{estimated})/I_{expected})$ of mobile F2 and F3 atoms at 64°C in $La_{1-x}Ba_xF_{3-x}$ solid solution increases with x from x = 0.03 (**Table 3**). These F1-F2,3 exchanges being moderate at 64°C, especially for the samples with resolved F2 and F3 NMR resonances (x = 0.03 and x = 0.05), our ^{19}F MAS NMR spectra do not allow to evidence a difference between F1-F2 and F1-F3 exchanges.

At the opposite, Grey et al. have shown by variable temperature ^{19}F MAS NMR on LaF_3 and $La_{0.99}Sr_{0.01}F_{2.99}$ that F1-F3 exchanges are faster than F1-F2 exchanges since the relative intensity of the NMR line assigned to F3 starts to decrease at lower temperatures than the one assigned to F2.[43] Owing to the absence of mobile F2 and F3 atoms for x = 0.03, the shift that affects the F1 peak can only be due to the substitution of La atoms by Ba atoms for this composition.

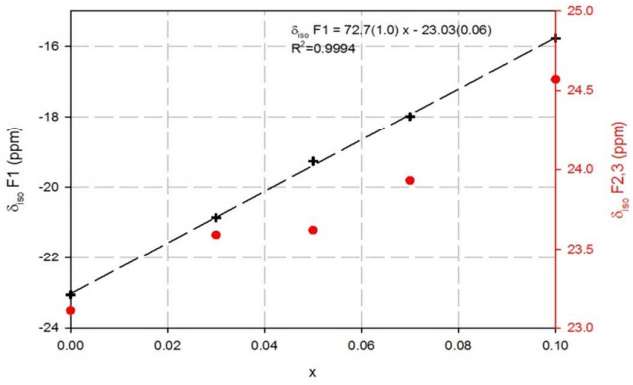

Fig. 9 Average and weighted ^{19}F δ_{iso} values of the NMR resonances used for the fits and assigned to F1 (black) and to F2 and F3 (red) in $La_{1-x}Ba_xF_{3-x}$ as a function of x. The dashed black line represents the calculated linear correlation for the ^{19}F δ_{iso} values of the NMR resonances assigned to F1 and corresponds to the equation reported on the graph.

For the following compositions, this substitution has also a significant impact on the chemical shift; the variation of the chemical shift is coherent with the larger δ_{iso} value of BaF_2 (-14.3 ppm[56], CN = 4, 2.683 Å[65]) as compared with the δ_{iso} value of F1 in LaF_3 (-23.1 ppm, CN = 4, 2.458 Å, 2.489 Å, 2.638 Å and 3.003 Å[16]). For the three-fold coordinated F2 and F3 atoms, the Ba substitution has a lower impact on the δ_{iso} values than on four-fold coordinated F1 atom: the short F2,3-La bond lengths (2.417 and 2.444 Å in LaF_3) cannot be accommodated by Ba atom. A smaller increase with x of the average and weighted ^{19}F δ_{iso} values of F2 and F3 atoms (in comparison with F1) is then evidenced (**Fig. 9**). However, according to Düvel *et al.*, the chemical shift of F2,3 decreases when x increases.[50] This disagreement comes from their determination of these chemical shifts from the maxima of asymmetric lines. The shoulder, which has not been observed by Düvel *et al.*,[50] has been assigned by Rongeat *et al.*[35] to "F anions from more disordered regions" but there is no obvious link between disorder and increase of chemical shifts. We assign this shoulder for x = 0.03 and x = 0.05 to a part of the F2 and F3 atoms surrounded by two La atoms and one Ba atom since its relative intensity (**see ESI**) is inferior to the probability of occurrence of the F2,3La_2Ba species (**Table 4**). Indeed, whatever the x value, the NMR resonances assigned to F2 and F3 overlap and they broaden when x increases. For x > 0.05, F2 and F3 resonances are no longer resolved in relation with increasing disorder and in agreement with F2 and F3 sites becoming similar (see F2-(La,Ba) and F3-(La,Ba) bond lengths on **Fig. 6**).

Further insights on chemical exchange processes can be obtained with the 2D EXSY NMR experiment[47,67-69] since a

Table 3 Relative intensities (I, %) of the ^{19}F NMR resonances assigned to F1 and F2,3, expected from formulation considering fluorine vacancies on F1 site and estimated from the fits of the NMR spectra recorded at 64°C (**see ESI**) and fractions of mobile F2 and F3 atoms (%) in $La_{1-x}Ba_xF_{3-x}$ compounds

x	0.03		0.05		0.07		0.10	
Site	F1	F2,3	F1	F2,3	F1	F2,3	F1	F2,3
Expected I	66.3	33.7	66.1	33.9	65.9	34.1	65.5	34.5
Estimated I	66.4	33.6	67.8	32.2	68.3	31.7	69.4	30.6
Mobile F2 and F3 atoms	0.2		5.0		7.1		11.3	

Table 4 Probabilities of occurrence (%) of the $FLa_{4-y}Ba_y$ (F = F1) and $FLa_{3-y}Ba_y$ (F = F2 or F3) species in $La_{1-x}Ba_xF_{3-x}$, based on a random distribution of Ba on the 6f site.

x	F site	FLa_4	FLa_3Ba	FLa_2Ba_2	$FLaBa_3$	FBa_4
0.03	F1	88.5	11.0	0.5	0.0	0.0
0.05	F1	81.5	17.1	1.4	0.0	0.0
0.07	F1	74.8	22.5	2.5	0.1	0.0
0.10	F1	65.6	29.2	4.9	0.4	0.0
x	F site	FLa_3	FLa_2Ba	$FLaBa_2$	FBa_3	
0.03	F2 or F3	91.3	8.5	0.3	0.0	
0.05	F2 or F3	85.7	13.5	0.7	0.0	
0.07	F2 or F3	80.4	18.2	1.4	0.0	
0.10	F2 or F3	72.9	24.3	2.7	0.1	

greater range of correlation times can be accessed. To avoid the presence of a cross-correlation peak due to a ^{19}F spin diffusion process (*i.e.*, a magnetization transfer through homonuclear ^{19}F dipolar couplings)[70-73] ultrafast MAS (44 kHz) and short mixing times (≤ 5 ms) were employed.[73,74] EXSY NMR experiments were applied only to $La_{0.97}Ba_{0.03}F_{2.97}$ and $La_{0.95}Ba_{0.05}F_{2.95}$ because for x > 0.05, F2 and F3 resonances are no longer resolved. The results are similar for both compositions and only the spectra of $La_{0.97}Ba_{0.03}F_{2.97}$, recorded at 40°C and with different mixing times (**Fig. 10**), are then discussed. At short mixing delay (100 µs), the spectrum (not shown) contains only diagonal peaks. For a longer mixing time of 250 µs (**Fig. 10a**), F1 and F2,3 cross-peaks are observed, revealing chemical exchange between the corresponding sites on the time scale of the mixing time (with a correlation time 100 µs < τ_c < 250 µs).

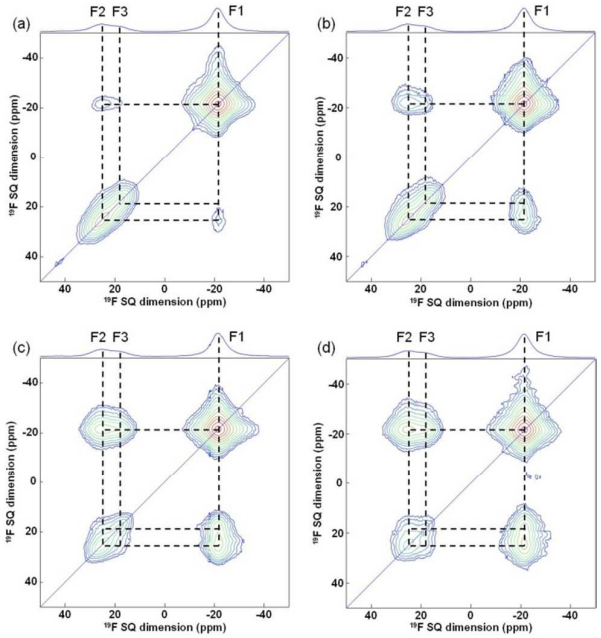

Fig. 10 2D ^{19}F MAS (44 kHz) EXSY spectra of $La_{0.97}Ba_{0.03}F_{2.97}$ recorded at 40°C and with mixing times of (a) 250 µs, (b) 500 µs, (c) 2 ms and (d) 5 ms. Top spectra, on which ^{19}F NMR lines are labeled, are the full projection on the ^{19}F MAS dimension. The thick solid line indicates the diagonal of the spectra and dash lines show fluorine-fluorine cross-correlations.

As expected, (**Fig. 10**), the cross peaks become more intense compared to the diagonal peaks when the mixing interval increases.[66] The spectra recorded with the longest mixing times (**Fig. 10 c and d**) also evidence cross-peaks between F2 and F3 resonances revealing, for the first time, chemical exchange between the corresponding sites, with a correlation time τ_c < 2 ms. Direct F2-F3 chemical exchange being unlikely since the shortest F2-F3 distances are equal to 4.178 Å, F2-F3 chemical exchange requires two successive jumps through F1, and then appears for longer mixing times. Unfortunately, no difference between F1-F2 and F1-F3 exchanges is evidenced from 2D EXSY MAS ^{19}F NMR spectra for the studied $La_{1-x}Ba_xF_{3-x}$ solid solutions. One possible explanation is that the intensity of the F1-F3 exchange remains too low (in part as a result of the low multiplicity of F3 atom) to emerge from the background noise for selective F1-F3 exchange mixing times (such that F1-F2 exchange does not occur).

3.4 Anion conductivity

All impedance diagrams at 25°C present a similar profile to that of **Fig. 11** whatever the composition of the samples $La_{1-x}Ba_xF_{3-x}$ (x = 0.03, 0.05, 0.07 and 0.10)**.** They are composed of two depressed semi-circles and a straight line at low frequency, due to polarization phenomena at the ion-blocking electrodes. The diagrams were fitted using an equivalent circuit based on two resistances and capacities in parallel, associated in series (**inset in Fig. 11**) for the electrolyte contribution. The straight line corresponding to the blocking electrode was also fitted using a CPE element in serie. The high and medium frequency semi-circles were assigned to the impedance of the bulk (B) and the grain boundaries (GB) contributions, respectively.

The conductivity was determined from the ceramic resistance ($R_{pellet} = R_B + R_{GB}$) according to the equation: $\sigma = \left(1/R_{pellet}\right) * e/S$ (e is the thickness and S the surface of the pellet). The Arrhenius-type law $\sigma.T = \sigma_0.e^{(-E_a/RT)}$, in which σ_0 is the pre-exponential constant factor, is satisfied for all 4 samples as shown in **Fig.** 12. The activation energy E_a together with the conductivity σ at room temperature (RT) are reported in **Table 5** (see **ESI**).

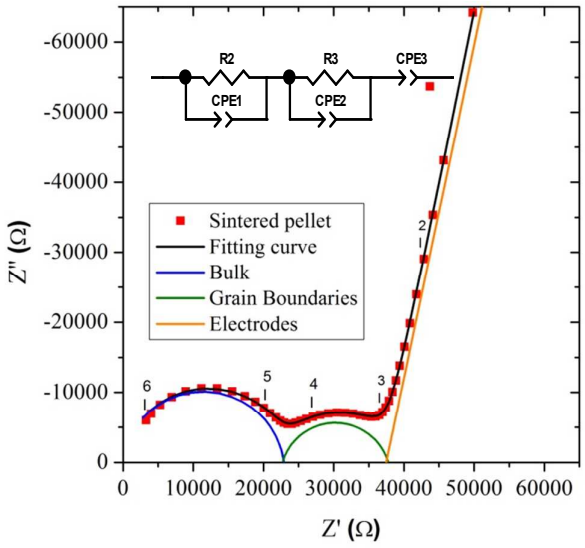

Fig. 11 Impedance diagram obtained at 25°C for a sintered pellet of $La_{0.95}Ba_{0.05}F_{2.95}$. Numbers indicate the log of the measurement frequency (e.g. 5 <=> 10^5 Hz). Inset: equivalent circuit used to fit the experimental data.

It can first be outlined that the ionic conductivity values at RT are very close to those reported previously on single crystals (≈ 6.10^{-5} vs 10^{-4} S.cm^{-1} at RT for $La_{0.93}Ba_{0.07}F_{2.93}$)[23] and almost two orders of magnitude higher than those reported on cold-pressed pellets[35]. The activation energy values lie between 0.2 and 0.4 eV. The maximum of conductivity at RT is observed for a composition close to x = 0.05-0.07 as previously reported (see introduction). Two implemented shaping processes of powdered $La_{0.95}Ba_{0.05}F_{2.95}$ were tested and compared to the sintering process at 900°C: cold uniaxial pressing and cold uniaxial and isostatic pressing (see 2.5). For the UP pellets, the obtained impedance diagrams were quite different to that of sintered pellets: only one semi-circle was observed at room temperature and the polarization line was scarcely visible.

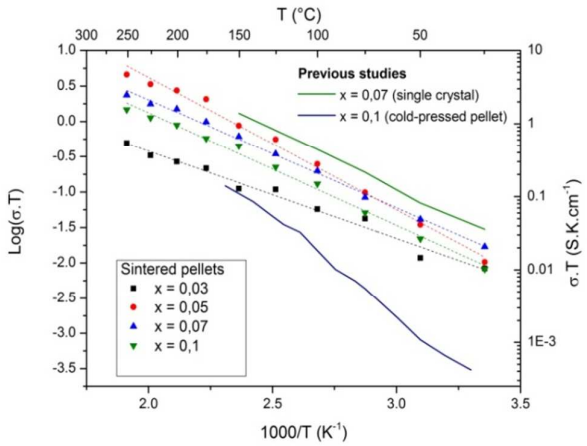

Fig. 12 Arrhenius plot of the conductivity for the $La_{1-x}Ba_xF_{3-x}$ samples synthesized by ceramic way and shaped by cold-uniaxial pressing, cold-isostatic pressing and sintering (dots + fitting lines). The values taken from the previous studies are represented by the green[23] and blue[35] lines.

Table 5 Activation energy E_a and conductivity σ of sintered $La_{1-x}Ba_xF_{3-x}$.

x	0.03	0.05	0.07	0.1
Ea (eV)	0.21	0.34	0.26	0.28
σ at RT (10^{-5} S.cm^{-1})	2.80	4.50	5.71	2.70

The IP pellets led to similar Nyquist diagrams but with better-defined polarization line and semi-circle (**ESI**).The deduced ionic conductivities are very low. The activation energies are slightly higher than that of the sintered sample (**Table 6**). As reported on **Fig. 13**, the IP pressing increases the conductivity of UP pellet by a factor 4 but the conductivity remains far from that of the sintered pellet. Due to the measurements temperature rise, the losses in fitting precision were ever higher above 150°C. Assuming this, the main capacity deduced from the impedance diagrams was close to $C_B = 10^{-10}$ F for the first semi-circle of the sintered pellet. Such capacitances could be assigned to the mobility of vacancies in the bulk, whereas their mobility in the grain boundaries is seemingly visible in the second semi-circle ($C_{GB} \approx 2.10^{-9}$F). The stability of the bulk capacity allows also to consider the $La_{0.95}Ba_{0.05}F_{2.95}$ product chemically stable over temperature in our low measurements range (**ESI**). However, the relaxation frequency data are mostly related to the inter-granular phenomena, as they always correspond to frequencies lower than in the grains (100 times lower for the sintered pellet). These GB-frequencies are thermally activated and show an Arrhenius-type behaviour (**ESI**).

The inter-grain contact area induced by cold pressing methods is clearly insufficient to insure optimal conduction paths. Even if the isostatic pressing reduces the porosity, it fails to allow chemical bonding between grains. A sintering step is then necessary to reach sufficient conductivities for RT FIB application.

Table 6 Influence of the shaping process on the activation energy E_a and conductivity σ of $La_{0.95}Ba_{0.05}F_{2.95}$.

Sample parameters	Uniaxial pressing	Uniaxial and isostatic pressing	Both pressing and sintering
Ea (eV)	0.36	0.43	0.34
σ at RT (10^{-5} S.cm^{-1})	0.041	0.178	4.50

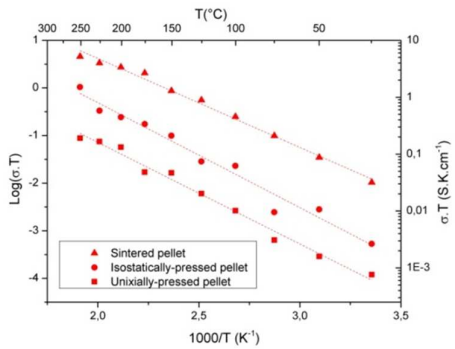

Fig. 13 Arrhenius plot of the conductivity for an only cold-uniaxial pressed pellet, a cold-uniaxial and cold-isostatic pressed pellet and a sintered pellet of $La_{0.95}Ba_{0.05}F_{2.95}$.

Conclusions

From X-ray and neutron diffraction experiments, accurate cell parameters ($x \leq 0.15$), obeying to Vegard's laws, and atomic position parameters ($x = 0.03$, 0.07 and 0.10) were determined for the tysonite-type solid solutions $La_{1-x}Ba_xF_{3-x}$. The samples were prepared by solid state synthesis, eventually followed by water quenching. The chemical pressure induced by large Ba^{2+} cations leads to an increase of the unit cell parameters. Anionic vacancies are localized on the F1-site that is the main contributor to fluorine mobility. From F-(La,Ba) distances, the F3 subnetwork contribution is assumed to be higher than that of F2 subnetwork for $x < 0.10$. A small variation of the buckling of $_\infty[La_{1-x}Ba_xF]^{2-x}$ layers and no significant evolution of the distorted tetrahedral environment of F1 are observed. The crossover of F1-F1,2,3 distances close to 2.7 Å together with a smaller dispersion of F1-F1,2,3 distances are the only structural features which could explain the conductivity maximum at $x \approx 0.05$-0.07. The ^{19}F MAS NMR spectra show the occurrence of F1-F2,3 exchanges in the $La_{1-x}Ba_xF_{3-x}$ solid solutions, at least for $x > 0.03$, at 64°C. The fraction of mobile F2 and F3 atoms increases with x from $x = 0.03$. 2D EXSY NMR spectra of $La_{0.97}Ba_{0.03}F_{2.97}$ reveal chemical exchange between F1 and F2,3 sites ($100\ \mu s < \tau_c < 250\ \mu s$) and, for the first time, chemical exchange between F2 and F3 sites ($\tau_c < 2$ ms) requiring two successive jumps. The ionic conductivity on sintered pellets is maximum around $x = 0.05$-0.07, in agreement with most of the previous work on single crystals. Moreover, when considering the feasibility of FIBs, we stressed the point of the usefulness of sintering to reach high ionic conductivity values. The cold pressing methods are clearly insufficient to reach ionic conductivity required for FIB electrolytes. This study is currently used as referential for the investigation of nanostructuration of $La_{1-x}Ba_xF_{3-x}$ solid solutions

Acknowledgements

This work is partly based on experiments performed at the Swiss spallation neutron source SINQ, Paul Scherrer Institute, Villigen, Switzerland.

The authors would like to thank the French National Research Agency for the financial support (FLUOBAT-ANR-12-PRGE-0009-01) and the doctoral and postdoctoral grants of J. Chable and B. Dieudonné, respectively. The authors are also indebted to Dr. A. Jouanneaux (IMMM) for his help with Rietveld refinements (neutron diffraction) and to Pr. J. Dittmer and Pr. J. Emery (IMMM) for their help with EXSY NMR experiments. Finally, special thanks are due to Dr M. Chennabasappa and Dr N. Penin (ICMCB) for the neutron diffraction experiments, to A.-M. Mercier (IMMM) for highly appreciated technical support and to M. Duttine (ICMCB) for the help with the writing.

References

1 J.-M. Tarascon and M. Armand, *Nature*, 2001, **414**, 359–367.
2 J. B. Goodenough and Y. Kim, *Chem. Mater.*, 2010, **22**, 587–603.
3 R. van Noorden, *Nature*, 2014, **507**, 26–28.
4 J. Christensen, P. Albertus, R. S. Sanchez-Carrera, T. Lohmann, B. Kozinsky, R. Liedtke, J. Ahmed and A. Kojic, *J. Electrochem. Soc.*, 2011, **159**, R1–R30.
5 V. Palomares, P. Serras, I. Villaluenga, K. B. Hueso, J. Carretero-González and T. Rojo, *Energy Environ. Sci.*, 2012, **5**, 5884–5901.
6 M. Anji Reddy and M. Fichtner, *J. Mater. Chem.*, 2011, **21**, 17059–17062.
7 W. Baukal, *Ger. Offen.*, 1971, GWXXBX DE 2017128.
8 J. H. Kennedy and J. C. Hunter, *J. Electrochem. Soc.*, 1976, **123**, 10–14.
9 C. Lucat, PhD Thesis, Université de Bordeaux 1, 1976).
10 N. I. Sorokin and B. P. Sobolev, *Crystallogr. Rep.*, 2007, **52**, 842–863.
11 L. N. Patro and K. Hariharan, *Solid State Ionics*, 2013, **239**, 41–49.
12 J.-M. Réau and J. Grannec, in *Inorganic Solid Fluorides, Chemistry and Physics*, ed. P. Hagenmuller, Academic Press, 1985, ch. 12, 423–467.
13 E. I. Ardashnikova, V. A. Prituzhalov and I. B. Kutsenok, in *Functionalized Inorganic Fluorides*, ed. A. Tressaud, Wiley-Blackwell, Chichester, 2010, ch. 14, 423–468.
14 M.S. Frant and J.W. Ross, *Science*, 1966, **154**, 1553–1555.
15 J. W. Fergus, *Sens. Actuators, B*, 1997, **42**, 119–130.
16 A. Zalkin and D. H. Templeton, *Acta Crystallogr. B*, 1985, **41**, 91–93.
17 A. Roos, *Mater. Res. Bull.*, 1983, **18**, 405–409.
18 A.P. Dudka, A.A. Loshmanov and B.P. Sobolev, *Crystallogr. Rep.*, 1998, **43**, 557–564.
19 R.H. Nafziger, N. Riazance, *J. Am. Ceram. Soc.*, 1972, **55**, 130-134.
20 B.P. Sobolev, N.L. Tkachenko, *J. Less-Common Met.*, 1982, **85**, 155-170.
21 A. Roos, J. Schoonman, A. F. Aalders, A. F. M. Arts and H. W. de Wijn, *Solid State Ionics*, 1983, **9&10**, 571–574.
22 A. Roos and J. Schoonman, *Solid State Ionics*, 1984, **13**, 205–211.
23 A. Roos, F.C.M. van de Pol, R. Keim and J. Schoonman, *Solid State Ionics*, 1984, **13**, 191–203.
24 A. Roos, J. Schoonman and D. Franceschetti, *J. Phys. Chem. Solids*, 1985, **46**, 645–653.
25 A. Roos, J. Schoonman, M. Buijs and K. E. D. Wapenaar, *J. Phys. Chem. Solids*, 1985, **46**, 655–664.
26 A. Roos, D. Franceschetti and J. Schoonman, *Solid State Ionics*, 1984, **12**, 485–491.
27 N. I. Sorokin, E. A. Krivandina, Z. I. Zhmurova, B. P. Sobolev, M. V. Fominykh and V.V. Fistul, *Phys. Solid State*, 1999, **41**, 573–575.
28 N. I. Sorokin and B. P. Sobolev, *Russ. J. Electrochem.*, 2007, **43**, 398–409.
29 N. I. Sorokin and B. P. Sobolev, *Phys. Solid State*, 2008, **50**, 416–421.
30 N. I. Sorokin, A. N. Smirnov, P. P. Fedorov and B. P. Sobolev, *Russ. J. Electrochem.*, 2009, **45**, 606–608.
31 N. I. Sorokin, N. A. Ivanovskaya and B. P. Sobolev, *Crystallogr. Rep.*, 2014, **59**, 248–251.
32 N. I. Sorokin, B. P. Sobolev, E. A. Krivandina and Z. I. Zhmurova, *Crystallogr. Rep.*, 2015, **60**, 123–129.
33 B. P. Sobolev and N. I. Sorokin, *Crystallogr. Rep.*, 2014, **59**, 807–830.
34 L. Zhang, M. Anji Reddy and M. Fichtner, *Solid State Ionics*, 2015, **272**, 39–44.
35 C. Rongeat, M. Anji Reddy, R. Witter and M. Fichtner, *ACS Appl. Mater. Interfaces*, 2014, **6**, 2103–2110.

36 A. F. Aalders, A. Polman, A. F. M. Arts and H. W. De Wijn, *Solid State Ionics*, 1983, **9&10**, 539–542.
37 A. F. Aalders, A. F. M. Arts and H. W. De Wijn, *Phys. Rev. B*, 1985, **32**, 5412-5423.
38 I. Brach and H. Schulz, *Solid State Ionics*, 1985, **15**, 135–138.
39 M. A. Denecke, W. Gunsser, A. F. Privalov and I. V. Murin, *Solid State Ionics*, 1992, **52**, 327–331.
40 A. F. Privalov, H.-M. Vieth and I. V. Murin, *J. Phys. Condens. Matter*, 1994, **6**, 8237–8243.
41 C. Hoff, H.-D. Wiemhöfer, O. Glumov and I. V. Murin, *Solid State Ionics*, 1997, **101-103**, 445–449.
42 D. Kruk, O. Lips, P. Gumann, A. Privalov, F. Fujara, *J. Phys.: Condens. Matter*, 2006, **18**, 1725–1741.
43 F. Wang and C. P. Grey, *Chem. Mater.*, 1997, **9**, 1068–1070.
44 F. Fujara, D. Kruk, O. Lips, A. Privalov, V. Sinitsyn and H. Stork, *Solid State Ionics*, 2008, **179**, 2350–2357.
45 L. C. M. Van Gorkom, J. M. Hook, M. B. Logan, J. V. Hanna and R. E. Wasylishen, *Magn. Reson. Chem.* 1995, **33**, 791–795.
46 A. Bielecki, D. P. Burum, *J. Magn. Reson. Ser. A*, 1995, **116**, 215–220.
47 J. Jeener, B. H. Meier, P. Bachmann, R. R. Ernst, *J. Chem. Phys.*, 1979, **71**, 4546–4553.
48 D. States, R. Haberkorn, D. Ruben, *J. Magn. Reson.*, 1982, **48**, 286–292.
49 D. Massiot, F. Fayon, M. Capron, I. King, S. Le Calvé, B. Alonso, J. O. Durand, B. Bujoli, Z. Gan, G. Hoatson, *Magn. Reson. Chem.*, 2002, **40**, 70–76.
50 A. Düvel, J. Bednarcik, V. Sepelak and P. Heitjans, *Journal J. Phys. Chem. C*, 2014, **118**, 7117–7129.
51 X'Pert Highscore Plus, 2004, **v. 2.0a (2.0.1)**, ed. PANalytical B.V., Almelo, The Netherlands.
52 J. Rodriguez-Carvajal, 1998, LLB (CEA-CNRS), **v.3.5d**.
53 R. D. Shannon, *Acta Crystallogr., Sect. A*, 1976, **32**, 751–767.
54 T. Takahashi, H. Iwahara, T. Ishikawa, *J. Electrochem. Soc.*, 1977, **124**, 280-284.
55 B. Dieudonné, J. Chable, F. Mauvy, S. Fourcade, E. Durand, E. Lebraud, M. Leblanc, C. Legein, M. Body, V. Maisonneuve, A. Demourgues, *J. Phys. Chem. C*, 2015, submitted.
56 A. Sadoc, M. Body, C. Legein, M. Biswal, F. Fayon, X. Rocquefelte, F. Boucher, *Phys. Chem. Chem. Phys.* 2011, **13**, 18539–18550.
57 F. Wang, C. P. Grey, *Chem. Mater.*, 1998, **10**, 3081–3091.
58 R. E. Youngman, C.M. Smith, *Phys. Rev. B*, 2008, **78**, 014112.
59 A. Picinin, R. R. Deshpande, A. S. S. de Camargo, J. P. Donoso, J. P. Rino, H. Eckert, M. A. P. Silva, *J. Chem. Phys.*, 2008, **128**, 224705.
60 G. Cho, C.-N. Chau, J.-P. Yesinowski, *J. Phys. Chem. C*, 2008**, 112***,* 6165–6172.
61 A. Düvel, S. Wegner, K. Efimov, A. Feldhoff, P. Heitjans, M. Wilkening, *J. Mater. Chem.*, 2011, **21**, 6238–6250.
62 A. Düvel, B. Ruprecht, P. Heitjans, M. Wilkening, *J. Phys. Chem. C*, 2011, **115**, 23784–23789.
63 C. Rongeat, M. A. Reddy, R. Witter and M. Fichtner, *J. Phys. Chem. C*, 2013, **117**, 4943–4950.
64 T. Krahl, G. Scholz, E. Kemnitz, *J. Phys. Chem. C*, 2014, **118**, 21066−21074.
65 A. S. Radtke, G. E. Brown, *Am. Mineral.*, 1974, **59**, 885−888.
66 M. H. Levitt, *Spin Dynamics: Basics of Nuclear Magnetic Resonance*; John Wiley & Sons, LTD: New York, 2000.
67 S. Chaudhuri, F. Wang, C. P. Grey, *J. Am. Chem. Soc.*, 2002, **124**, 11746-11757.
68 C. Martineau, F. Fayon, C. Legein, J.-Y. Buzaré, G. Corbel, *Chem. Mater.*, 2010, **22**, 1585–1594.
69 C. Martineau, F. Fayon, M. R. Suchomel, M. Allix, D. Massiot, F. Taulelle, *Inorg. Chem.*, 2011, **50**, 2644–2653.
70 D. Suter, R. R. Ernst, *Phys. Rev. B*, 1985, **32**, 5608–5627.
71 P. M. Henrichs, M. Linder, J. M. Hewitt, *J. Chem. Phys.*, 1986, **85**, 7077–7086.
72 A. Kubo, C. A. McDowell, *J. Chem. Phys.*, 1988, **89**, 63–70.
73 L.-S. Du, M. H. Levitt, C. P. Grey, *J. Magn. Reson.*, 1999, **140**, 242–249.
74 D. Reichert, T. J. Bonagamba, K. Schmidt-Rohr, *J. Magn. Reson.*, 2001, **151**, 129–135.